Energy 278 (2023) 127788

Contents lists available at ScienceDirect

Energy

journal homepage: www.elsevier.com/locate/energy

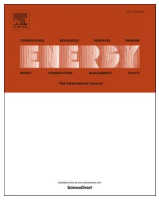

Adsorption characteristics of shale gas in organic–inorganic slit pores

Junqing Chen [a,b,c], Fujie Jiang [a,d,*], Qi Cong [b], Xiongqi Pang [a,d], Kuiyou Ma [a,d], Kanyuan Shi [a,d], Bo Pang [a,d], Dongxia Chen [a,d], Hong Pang [a,d], Xiaobin Yang [b], Yuying Wang [b], Bingyao Li [b]

[a] State Key Laboratory of Petroleum Resources and Prospecting, China University of Petroleum, Beijing, 102249, China
[b] Basic Research Center for Energy Interdisciplinary, College of Science, China University of Petroleum, Beijing, 102249, China
[c] Beijing Key Laboratory of Optical Detection Technology for Oil and Gas, China University of Petroleum, Beijing, 102249, China
[d] College of Geosciences, China University of Petroleum, Beijing, 102249, China

ARTICLE INFO

Handling Editor: Wojciech Stanek

Keywords:
Shale gas
Molecular simulation
Adsorption characteristics
Monte Carlo

ABSTRACT

With the gradual advancement of shale gas exploration and development technology, shale gas has replaced conventional oil and gas as the primary energy source. As the main occurrence form of natural gas in shale reservoirs, the adsorption state is always an important research topic for evaluating the gas-bearing property of shale reservoirs and improving shale gas recovery. However, at present, there are few studies on control factors and control mechanisms of adsorbed gas in organic–inorganic slit pores, with several unexplained control factors and mechanisms. Taking Songliao Basin shale as an example, molecular simulations are employed to investigate shale gas adsorption in organic–inorganic slit pores, the graphene and kaolinite rock matrix model is employed, and molecular dynamics simulations, particularly the grand canonical Monte Carlo simulation is studied for pore sizes of 2, 4, and 6 nm, The adsorption behavior of methane on heterogeneous shale surfaces at temperatures of 298, 323, 348, 373, and 398 K and pressures of 0.1, 5, 10, 15, and 20 MPa reveals the microscopic mechanism of shale gas adsorption in organic–inorganic slit pores at a molecular scale. The results show that as temperature and pressure increase simultaneously, methane is more strongly adsorbed on the surface of graphene than kaolinite, the number of methane molecules also gradually decreases, the root mean square of the displacement of methane and different surface forces between atoms exhibit certain regularity, and the adsorption capacity of the system is proportional to the changes in diameter within the system. Van der Waals energy and electrostatic energy in the system also increase gradually with changes in temperature and pressure, and electrostatic energy has a greater influence on the adsorption of the system than van der Waal energy. These findings provide ideas for the adsorption capacity of shale gas in organic–inorganic slit pores and are critical for the accurate evaluation of shale reservoir gas content and improvement of shale gas recovery.

1. Introduction

In recent years, oil and gas exploration and development and mass transfer efficiency have been extensively promoted, with all production options explored, to promote the development of high-quality shale oil and gas and other unconventional energy, with shale gas proven reserves reaching two trillion cubic meters by the end of 2020; however, the proven rate is only 5.72% of China's shale gas, which is still in the early stage of exploration and development [1]. Methane content in shale gas ranges from 70% to 90% [2–4], with adsorption and free methane being the most common occurrence states [5,6]. Methane is free in the shale pore space and adsorbs on the shale matrix surface [7]. The study of the adsorption state in shale gas is critical for improving shale gas recovery [8].

The composition of shale can be divided into organic matter and inorganic materials [9]. Organic matter is primarily composed of kerogen [10]. Inorganic materials are primarily composed of quartz and clay minerals, including kaolinite, montmorillonite, and illite [11]. Due to the complex composition of shale, its pore structure is complicated, and its pore types include pure organic pores, pure inorganic pores, and organic–inorganic pores [12]. According to the pore diameter of shale, it can be divided into micropores, mesopores, and macropores. Common shale pore shapes include slit pores, round pores, square pores, and triangular pores, among which slit pores are mostly found in the shale matrix [13]. Experimental analytical methods, including nuclear magnetic resonance methods and isothermal adsorption methods [14–19],

* Corresponding author. State Key Laboratory of Petroleum Resources and Prospecting, China University of Petroleum, Beijing, 102249, China
E-mail address: jfjhtb@163.com (F. Jiang).

https://doi.org/10.1016/j.energy.2023.127788
Received 24 October 2022; Received in revised form 26 April 2023; Accepted 8 May 2023
Available online 9 May 2023

as well as research methods from the macroscopic perspective to study the adsorption behavior of shale gas matrix, are common methods for studying the adsorption behavior of shale gas. However, due to the heterogeneity of continental shale and the high cost of the experiment, small amounts of experimental samples are insufficient to fully represent the actual circumstances of the underground conditions. Therefore, experimental methods have limitations, and it is impossible to study the adsorption characteristics of shale gas by various pore types from a microscopic perspective [20–23]. Molecular simulation technology can be used to solve the above problems and to reveal the microscopic mechanism of shale gas adsorption from the molecular scale [24–26].

Currently, few studies on the adsorption characteristics of shale gas in organic–inorganic pores have been conducted. Ji et al. [27] investigated the effects of five clay minerals on methane adsorption. The results show that the specific surface area of clay minerals is proportional to the adsorption capacity of methane. The adsorption capacity of the five clay minerals is ranked as montmorillonite > I-s mixing layer > Kaolinite > Chlorite > Illite. Aman. Sharma et al. [28] investigated the adsorption of methane and ethane in clay minerals with different pore sizes. The results show that as pressure increases, the density of methane increases gradually, and there is monolayer adsorption on both sides of the pore wall, but there is double adsorption on ethane. Huang et al. [29] used grand canonical Monte Carlo (GCMC) simulation to simulate the adsorption behavior of methane and carbon dioxide on four kerogen with different maturity. The results show that the adsorption energy of kerogen to gas is proportional to its maturity. However, molecular simulation technology has not been used to comprehensively and systematically calculate and theoretically study methane adsorption in organic–inorganic slit pores.

Under the same isothermal pressure and pore size conditions, Li [30] found that slit pores of calcite had a stronger ability to adsorb alkanes than cylindrical pores; Song et al. [31] investigated the adsorption of shale gas in organic matter pores of different shapes via GCMC simulations. The results showed that the adsorption concentration in slit pores was the highest due to the maximum Langmuir pressure, followed by the adsorption concentration in square pores, and the lowest in triangular pores. This is due to the large specific surface area of slit pores, which results in a strong adsorption capacity. Song et al. superimposed the simulated adsorption isotherms to obtain the adsorption isotherms of microporous carbon, and compared them with the experimental data of coal samples at the same temperature. The experimental isotherms were closer to the slit hole excess isotherms, while the excess isotherms predicted based on round and square holes underestimated the excess adsorption capacity. Therefore, in the molecular simulation results, the molecular model of the slit hole is more consistent with the reality. Moreover, Wang et al. [32,33] found that most slit pores exist in the shale matrix; Taking Qingshankou Formation shales in Songliao Basin as an example, the shales have mesoporous properties, and the pores are mainly fracture-like pores produced by plate particles aggregate [34]. Compared with other pore shapes, slit pores have larger surface area and porosity, which can store a large amount of methane in a small space. The formation of methane adsorption layer, the boundary between adsorption zone and free zone, and the distribution of methane in the X, Y and Z axes can be clearly and intuitively observed in slit pores. Thus, we selected slit pores as the simulated shale pore shape in this paper. According to previous studies [35,36], graphene is an important substitute material for studying gas adsorption mechanisms on the surface of organic minerals in the shale matrix [37], whereas kaolinite is more commonly used in various clay minerals and as the inorganic mineral surface of the shale matrix [38–40]. Therefore, in our study, graphene was used to represent organic minerals, and kaolinite was used to represent inorganic minerals to explore the adsorption of methane by organic and inorganic minerals in slit pores.

In this paper, molecular dynamics (MD) simulation and GCMC simulations were used to analyze the adsorption behavior of methane on graphene–kaolinite pores at slit sizes of 2, 4, and 6 nm, temperatures of 298, 323, 348, 373, and 398 K, and pressures of 0.1, 5, 10, 15, and 20 MPa. According to analysis results in terms of the interaction energy, diffusion coefficient, radial distribution function (RDF), relative concentration distribution, isothermal adsorption curve, and adsorption heat of the adsorption system, the adsorption characteristics of organic and inorganic surfaces differ. The findings of this research provide ideas for the adsorption capacity of shale gas in organic–inorganic slit pores, which are critical for accurate shale reservoir gas content evaluation and shale gas recovery improvement.

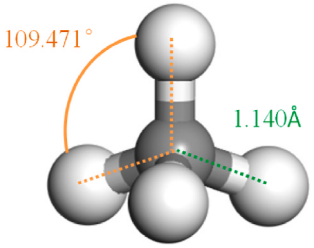

Fig. 1. Model of methane.

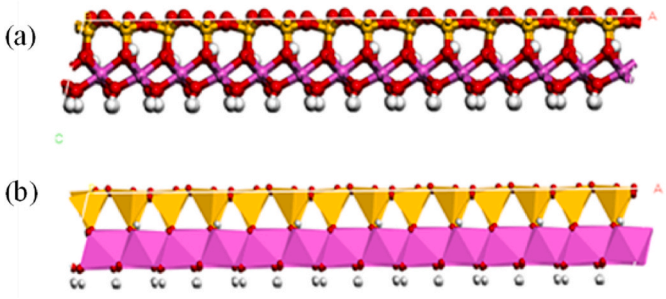

Fig. 2. Kaolinite. (a) Ball-and-stick model (b) polyhedron structure.

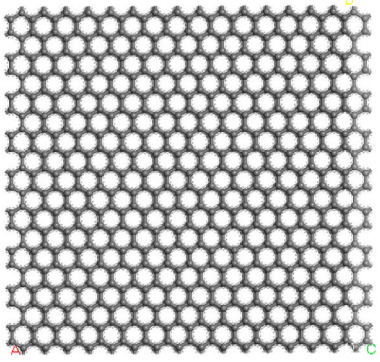

Fig. 3. Ball-and-stick model of graphene.

2. Models and simulation methods

2.1. Models

In this paper, the molecular model of methane adopts a ball-and-stick model [41,42] (Fig. 1), and the bond length and bond angle of the all-tom model are 1.140 Å and 109.471°, respectively. The molecular models of kaolinite and graphene are based on actual crystal structures. Kaolinite belongs to the triclinic crystal system and the space group 1P/1. The structural formula of kaolinite is $Al_4[Si_4O_{10}](OH)_8$. This structure belongs to the TO type (Fig. 2b). Strong hydrogen bonds (O–OH = 0.289 nm) strengthen bonds between structural layers [43–46]. The specific cell parameters of kaolinite are a = 5.15 Å, b =

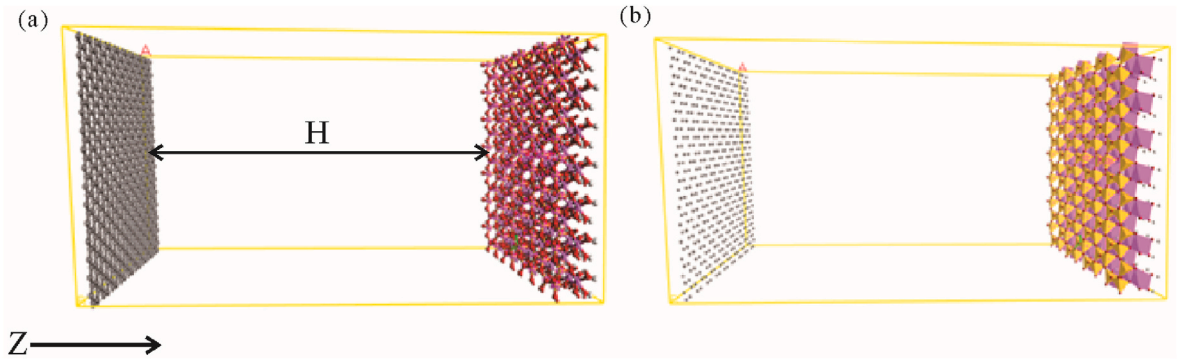

Fig. 4. Initial model. (a) Ball-and-stick model (b) polyhedron structure.

Fig. 5. Molecular model building flow chart.

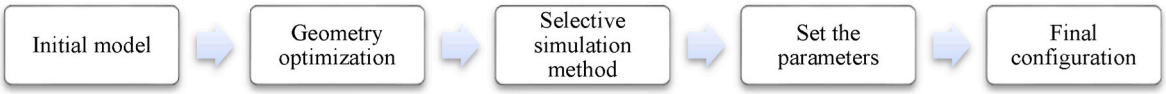

Fig. 6. Flow chart of molecular simulation calculation.

8.93 Å, c = 7.38 Å, α = 91.93°, β = 105.04°, γ = 89.79°, and Z = 1 [47]. The size of single-layer kaolinite is 36.47 Å × 37.04 Å × 7.38 Å (Fig. 2a). Graphene is a two-dimensional carbon material composed of a layer of carbon atoms packed closely periodically in a benzene ring structure (hexagonal honeycomb structure) (Fig. 3). The coordination number of carbon atoms is 3, the bond length between each two adjacent carbon atoms is 1.42 Å, and the included angle between bonds is 120°. The size of monolayer graphene is 36.47 Å × 37.04 Å. Fig. 4 illustrates the adsorption characteristics of organic–inorganic slit pores on shale gas. Along the Z-axis, graphene is on the left and kaolinite is on the right. The size of aperture H is defined as the distance between the O atom in the innermost layer of kaolinite and the C atom in the innermost layer of graphene. The process for building a molecular model with the Materails Studio software is shown in Fig. 5.

2.2. Simulation methods and details

Molecular simulation technology entails inputting a certain number of molecules into a computer to determine the molecular microstructure and macroscopical properties of materials. It mainly relies on Newtonian mechanics to simulate the motion of a molecular system and uses samples from different states of the molecular system to calculate the configuration integral of the system. On the basis of the configuration integral results, the thermodynamic quantity and other macroscopic properties of the system are further calculated. The goal is to attempt to replace the instantaneous average behavior of several particles with the long-term average behavior of a few particles. In this paper, MD and Monte Carlo (MC) simulations are used. The microscopic simulation calculation process is shown in Fig. 6. MD simulation can be used to analyze the diffusion and concentration distribution of adsorbents, as well as the changes in the force and energy between adsorbents and adsorbates. MC simulation can be used to obtain the adsorption heat and capacity of an adsorption system under different temperature and pressure conditions.

First, the GCMC method, which is widely used in the study of adsorption phase equilibria in adsorption systems, was adopted [48–51]. In the GCMC simulation, grand canonical ensembles are adopted. The chemical formula, volume, and temperature of the target gas are fixed, whereas the number of molecules and the amount of energy of the system vary. The chemical potential is a function of fugacity, which represents the effective pressure, and the Peng-Robinso (PR) equation of state is used to calculate fugacity [52–56].

Table 1
Main input parameters of Sorption modules.

Simulation Modules	Parameter	Input	Unit
Sorption	Task	Fixed pressure	MPa
	Method	Metropolis	/
	Equilibration steps	3,000,000	step
	Production steps	5,000,000	step
	Force field	Compass	/
	Charges	Forcefield assigned	
	Quality	Fine	
	Electrostatic summation method	Ewald	/
	van der Waals summation method	Atom-based	/
	Cutoff distance	15.5	Å

To investigate the methane adsorption of shale of Songliao Basin, the system parameters are set according to the actual geological conditions of Songliao Basin. According to the main temperature and pressure range [57,58] of the oil window stage of Songliao Basin, the temperature range of the system is set as 298–398 K, with a temperature interval of 25 K. The pressure range is set to 0.1–20 MPa, with a pressure interval of 5 MPa. This process can be realized using the Sorption module in Materials Studio software, and the overall distribution trend conforms to the Boltzmann distribution [59], generating a series of random configurations of microscopic particles. Specific parameter settings are listed in Table 1. Secondly, select adsorbed methane, input the fugacity value converted from PR equation, and then input the set temperature value to complete a simulation. The input value of the next simulation temperature will remain unchanged, and the pressure will be changed until the simulation of all pressures at the same temperature is completed. Then

Table 2
Main input parameters of Forcite modules.

Simulation Modules	Parameter	Input	Unit
Forcite	Task	Dynamics	/
	Ensemble	NVT	/
	Control method	Nose	/
	Time step	1.00	fs
	Number of steps	2,000,000	/
	Duration	2000	ps
	Force field	Compass	/
	Electrostatic summation method	Ewald	/
	van der Waals summation method	Atom-based	/
	Barostat	Berendsen	
	Total simulation time	2	ns

the next temperature value to be set will be input, and so on. The data obtained from the simulation will be analyzed and drawn. A total of 25 sets of GCMC simulations need to be completed in this paper. The isothermal adsorption curve, adsorption heat, and total adsorption capacity can be obtained via GCMC simulation.

MD simulation uses the final configuration simulated by GCMC for simulation calculation [48]. First, the model is geometrically optimized to achieve the equilibrium state of the system, and then MD simulation is performed in the NVT ensemble [60,61]. Five groups of temperature and pressure conditions are set for the simulation: 298 K and 0.1 MPa; 323 K and 5 MPa; 348 K and 10 MPa; 373 K and 15 MPa; 398 K and 20 MPa. The Forcite module in Materials Studio [62,63] can be used to describe non-bond interactions using the Lennard-Jones potential function [64,65]. In MD simulation, the pressure and temperature values are directly input. This paper needs to complete five MD simulations. Obtain the required data from the simulation result file to analyze the kinetic characteristics of the adsorption system. MD simulation can obtain the diffusion coefficient, RDF, energy change, and concentration distribution characteristics of gas adsorption in pores. Specific parameter settings are listed in Table 2.

3. Results and discussion

By using GCMC and MD simulations, MD simulation can analyze the diffusion of adsorbent molecules, concentration distribution, and the change of the force and energy between adsorbent and MD simulation. MC simulation can be used to obtain the adsorption and adsorption capacity of the adsorption system at different temperatures and pressures. Specific analysis is as follows.

3.1. MSD (mean square displacement)

The diffusion phenomenon describes how material molecules move from a high concentration area to a low concentration area until a uniform distribution is reached, with the rate proportional to the concentration gradient of the material [66]. It is a transport phenomenon based on molecular thermal motion and is a process in which molecules are transported from a high concentration region (or high potential) to a low concentration region (or low potential) through Brownian motion [67,68]. The diffusion phenomenon and several reports have shown that the molecules of all matter are constantly moving irregularly. The diffusion coefficient is one of the important standards for describing the molecular motion intensity [69]. According to Einstein's equations, the diffusion coefficient is 1/6 of the root mean square displacement of the slope, and the diffusion coefficient is proportional to the particle motion of time, which is inversely proportional to the shale adsorption ability. In terms of the diffusion coefficient, the more molecules within the system, the greater the degree of freedom and less adsorption [70]. The

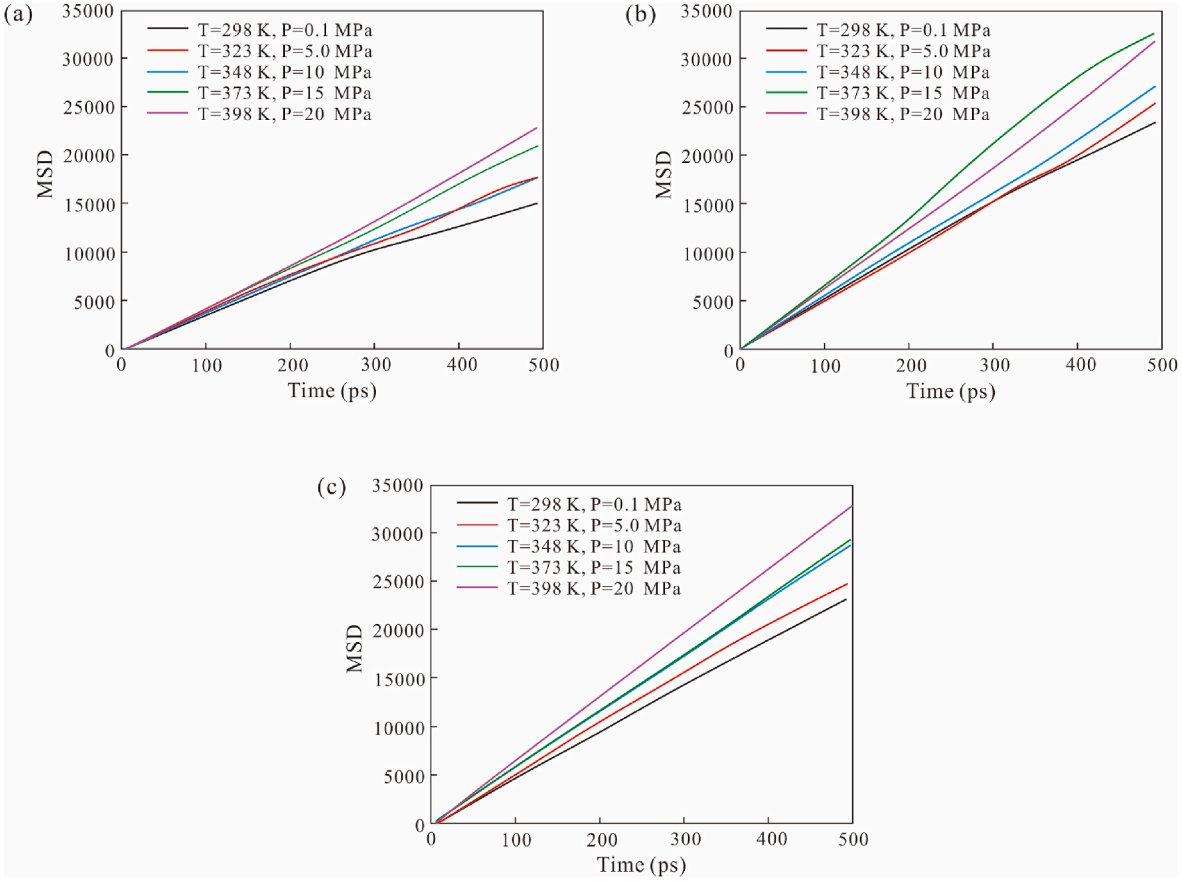

Fig. 7. Diffusion coefficient of methane at different temperatures and pressures. (a) Slit aperture of 2 nm; (b) Slit aperture of 4 nm; (c) Slit aperture of 6 nm.

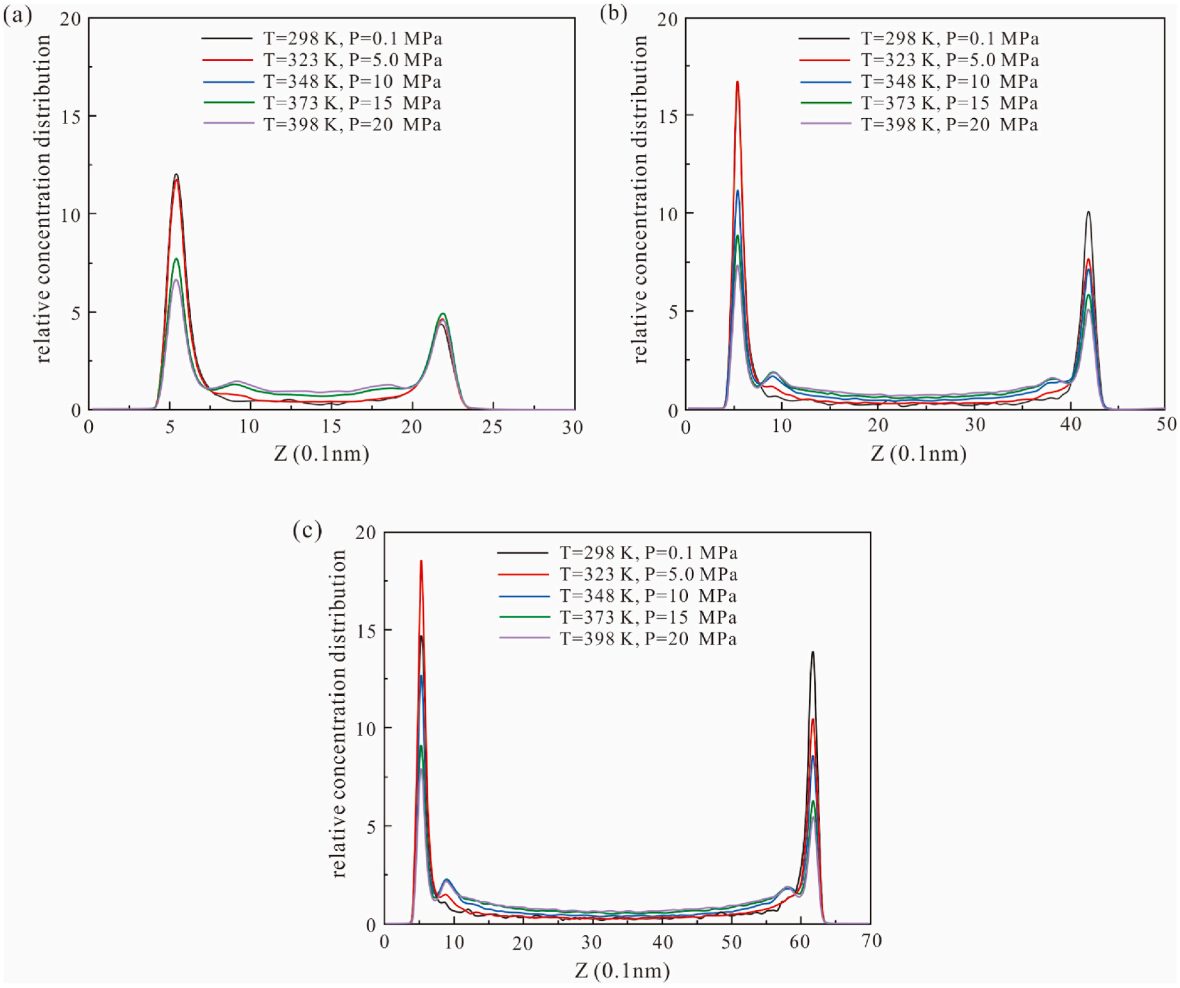

Fig. 8. Relative concentration distribution of methane molecules at different temperatures and pressures. (a) Slit aperture of 2 nm; (b) Slit aperture of 4 nm; (c) Slit aperture of 6 nm.

root mean square displacement indicates that the adsorbent molecule will move irregularly rather than in a fixed position [71]. The slope of root mean square displacement of the system is expressed as Eq. (1).

$$K_{\mathrm{MSD}} = \frac{1}{N}\sum_{i=1}^{N}[r_i(t) - r_i(0)]^2 \# \tag{1}$$

The self-diffusion coefficient is expressed as Eq. (2).

$$D = \frac{1}{6N}\lim_{t\to\infty}\frac{d}{dt}\sum_{i=1}^{N}[r_i(t) - r_i(0)]^2 \# \tag{2}$$

Then, the relationship between the slope of root mean square displacement and the self-diffusion coefficient is Eq. (3).

$$D = \frac{1}{6}K_{MSD} \# \tag{3}$$

Where, D is the self-diffusion coefficient of methane, m^2/s; K_{MSD} is the slope of the mean square displacement; t is the simulation time, s; N is the total number of methane molecules; N_t is the statistical average number of molecular dynamics steps, step; $r_i(t)$ is the real displacement of the centroid of the ith particle at time t, nm.

The root mean square displacement of methane molecules at different temperatures and pressures is shown in Fig. 7. At pore sizes of 2, 4, and 6 nm, the slope of the root mean square displacement of methane molecules is smallest at a temperature of 298 K and pressure of 0.1 MPa (Fig. 7a, b, and c), indicating that methane molecules in the system are most stable under such temperature and pressure conditions. With increasing temperature and pressure, the slope of the root mean square displacement of methane molecules is proportional to their change, indicating that the kinetic energy of methane molecules increases and the molecular thermal motion becomes more intense. At the same temperature and pressure, the value of the root mean square displacement of methane molecules increases gradually as the pore size increases. Skoulidas, A. I. et al. [72–74] also obtained a similar conclusion by MD simulation. Kazemi M et al. [3,75] believed that the diffusion coefficient of shale gas in organic graphene narrow pores decreased with the increase of pressure; Zhang T et al. [76] believes that the diffusion coefficient of organic pores increases with the increase of temperature and pressure, so the influence of temperature is greater; Chen C et al. [77] analyzed that in the clay mineral system, during the gas diffusion, the influence of pore size on the in-plane self-diffusion is more significant, which is consistent with our research.

3.2. Relative concentration distribution

As can be seen from the distribution space of methane in Fig. 8, methane molecules are distributed in parallel along the pore wall of the slit, forming an obvious adsorption layer. No methane molecules are distributed in the area closest to both sides of the pore wall, which can be considered an unadsorbed area. The distribution of methane molecules in organic–inorganic slit pores was further analyzed at a molecular scale, as well as its relative concentration. At different temperatures,

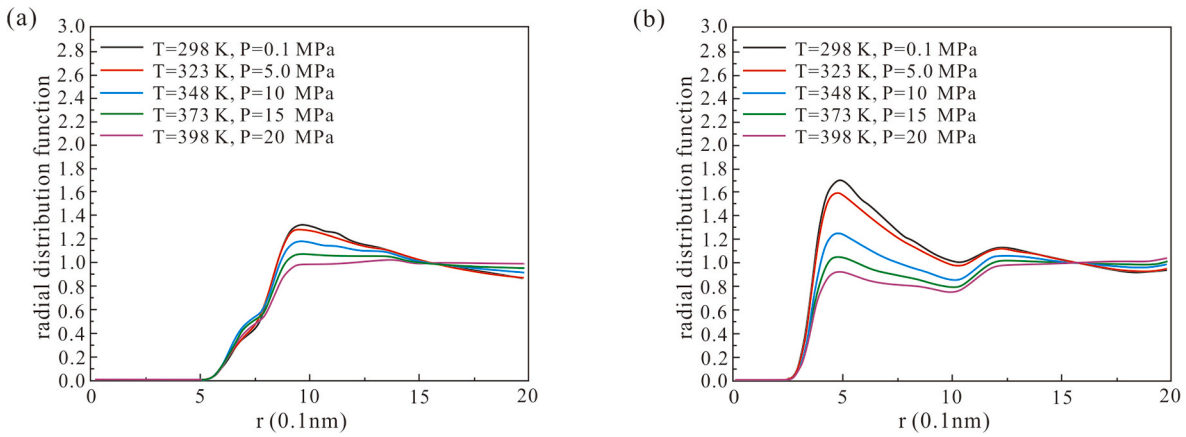

Fig. 9. RDF of methane molecules and each atom at different temperatures and pressures when pore diameter is 2 nm. (a) Methane and aluminum; (b) Methane and carbon.

pressures, and pore sizes, the relative concentration distribution of methane molecules along the Z-axis in Fig. 4 is shown in Fig. 8. As shown in Fig. 8, the relative concentration distribution trend is asymmetry. Sharma A et al. [78–80] found that the concentration of methane distribution in clay minerals and organic matter graphene slit pores was central symmetry, and the concentration of methane in organic pores was higher than that of clay minerals. On the graphene side closer to the origin of the Z-axis, the graphene surface relative concentration of methane molecules first adsorption layer was higher than that of the surface of the kaolinite, and in the slit on both sides of the aperture relative concentrations are usually the first adsorption layer and decreased with increasing temperature and pressure. When the temperature is between 298 K and 323 K and the pressure is between 0.1 and 5 MPa, the relative concentration of the first adsorption layer on the side of kaolinite does not decrease with increasing temperature and pressure (Fig. 8a). This is because the number of methane molecules in the system varies with the density of methane molecules in different volume spaces and under different temperature and pressure conditions. For example, with a pore diameter of 2 nm, the density of methane molecules in the system is 99.773 g/m^3 at 298 K and 0.1 MPa. The number of methane

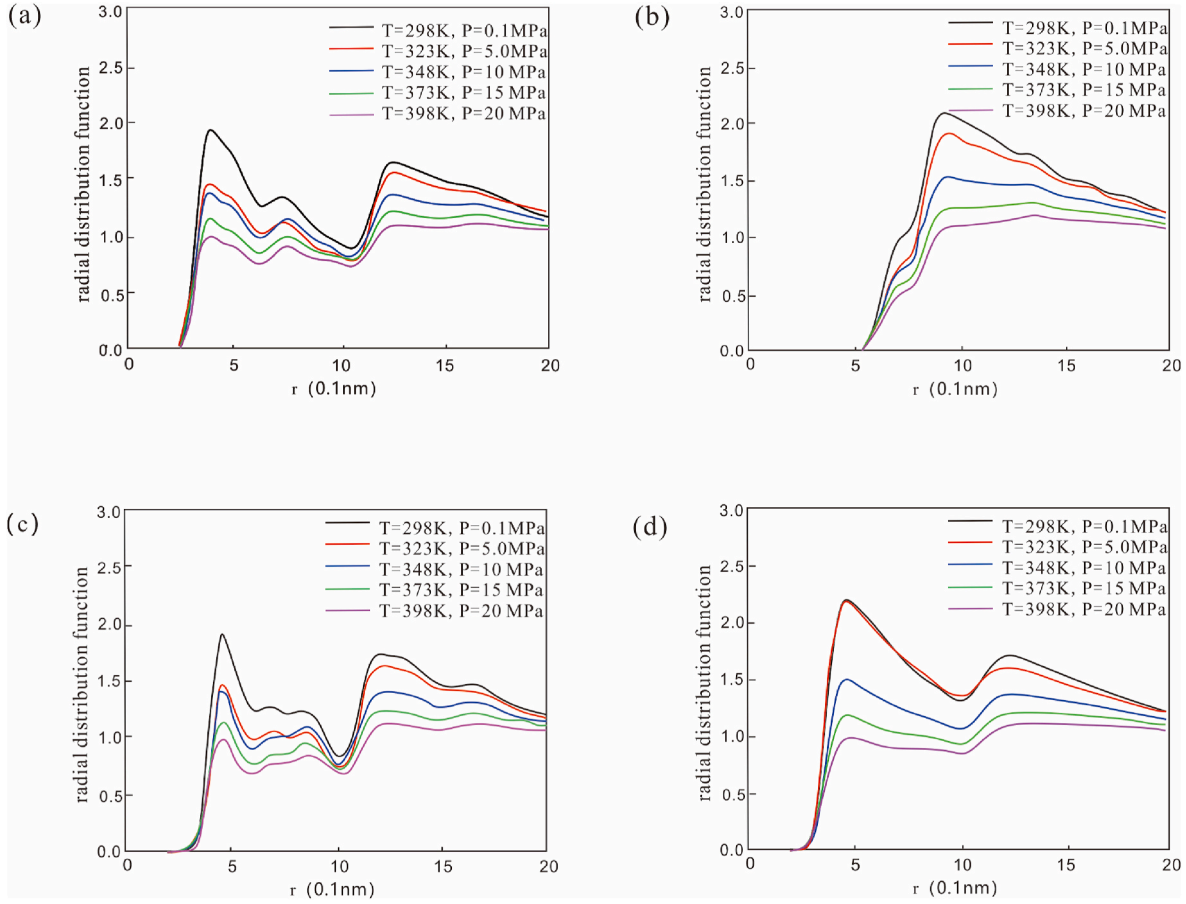

Fig. 10. RDF of methane molecules and each atom at different temperatures and pressures when pore diameter is 4 nm. (a) Methane and oxygen; (b) Methane and aluminum; (c) Methane and silicon; (d) Methane and carbon.

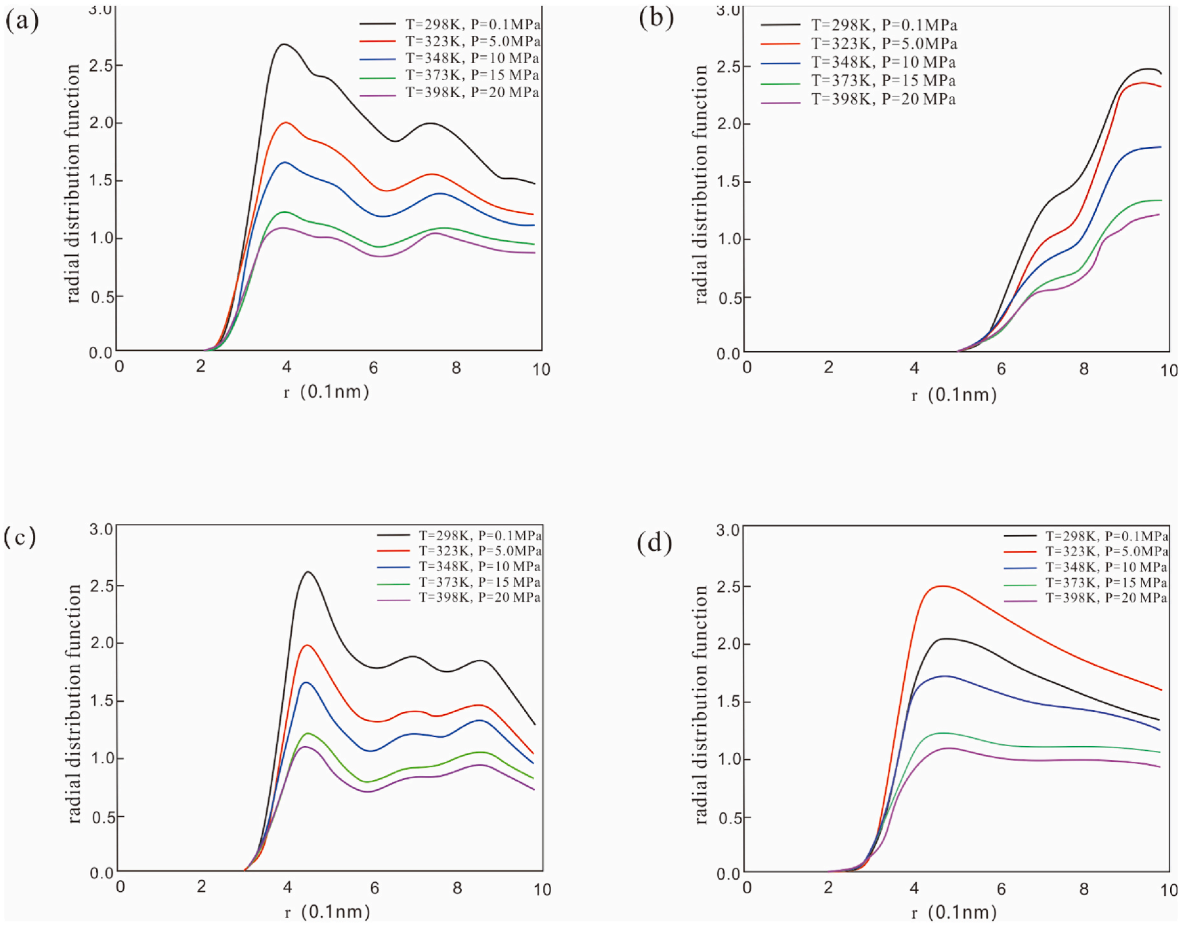

Fig. 11. RDF of methane molecules and each atom at different temperatures and pressures when pore diameter is 6 nm. (a) Methane and oxygen; (b) Methane and aluminum; (c) Methane and silicon; (d) Methane and carbon.

molecules in the system is fixed. The relative concentration of the first adsorption layer of methane molecules on the graphene side is too high, so the relative concentration of methane molecules on the kaolinite side is low. Similarly, as the number of methane molecules in the system remains constant, on the graphene side in Fig. 8b and (c), the relative concentration of the first adsorption layer of methane molecules at 323 K and 5 MPa is higher than that at 298 K and 0.1 MPa. This is because when the temperature is 298 K and the pressure is 0.1 MPa on the kaolinite side, the relative concentration of the first adsorption layer is significantly higher than that at 323 K and 5 MPa. At room temperature and pressure, there is only one adsorption layer on both sides of the pore wall; however, when the temperature is 323 K and the pressure is 5 MPa, the second adsorption layer of methane molecules begins to form on both sides of the slit under different pore sizes, and the relative concentration of the second adsorption layer is primarily influenced by pressure, which is proportional to the change in pressure. In general, with increasing pore size, the relative concentrations on both sides of the pore wall increase. When the pore size is 2, 4, and 6 nm, the relative concentrations of the first adsorption layer on the side of kaolinite are 4.5, 10.2, and 14.3, respectively, at a temperature of 298 K and a pressure of 0.1 MPa. The relative concentration of the first adsorption layer does not increase exponentially with increasing pore size. With increasing temperature and pressure, the relative concentration of the first adsorption layer of methane molecules is inversely proportional to it.

3.3. RDF (radial distribution function)

RDF can explain the distribution number density of particles within a certain range of the reference particle [81]. The RDF between C atoms in methane molecules and each atom on the pore wall surface is the commonly used method for analyzing the force between methane and graphene and kaolinite. At an aperture of 2 nm (Fig. 9), the number of methane molecules, graphene C atoms, and kaolinite alumina on eight surfaces on the surface of the body surface of Al atoms decreased with increasing temperature and pressure; however, when pressure is less than 5 MPa, the number of methane molecules and graphene C atoms on the surface of the peak increases. In conclusion, methane interacts with graphene more strongly than kaolinite. As shown in Fig. 10, when the pore size is 4 nm, methane molecules and kaolinite alumina on eight surfaces on the surface of the body surface of Al atoms and O, Si atoms on the surface of the silicon tetrahedron RDF are between the change in temperature and pressure is inversely proportional to, compared with kaolinite and aluminum oxide octahedral surface, methane molecules and kaolinite interaction on the surface of the silicon tetrahedron is stronger. The RDF of methane and graphene C atoms is also inversely proportional to the change in temperature and pressure. At 298 K and 0.1 MPa, the maximum peak value of C atoms on methane and graphene surfaces is 2.25. As shown in Fig. 11, when the pore size is 6 nm, changes in the number of methane molecules and Al atoms on the octahedral surface of kaolinite alumina and O and Si atoms on the tetrahedral surface of silicon are consistent with those at a pore size of 4 nm. The interaction force between the C atoms of methane molecules and graphene is strongest at 323 K and 5 MPa. This is also the reason for the highest relative concentration of methane molecules on the graphene side at this temperature and pressure, as shown in Fig. 8c.

As the system adsorbed the most methane molecules at 298 K and 0.1 MPa, it is necessary to further investigate the RDF of each atom on

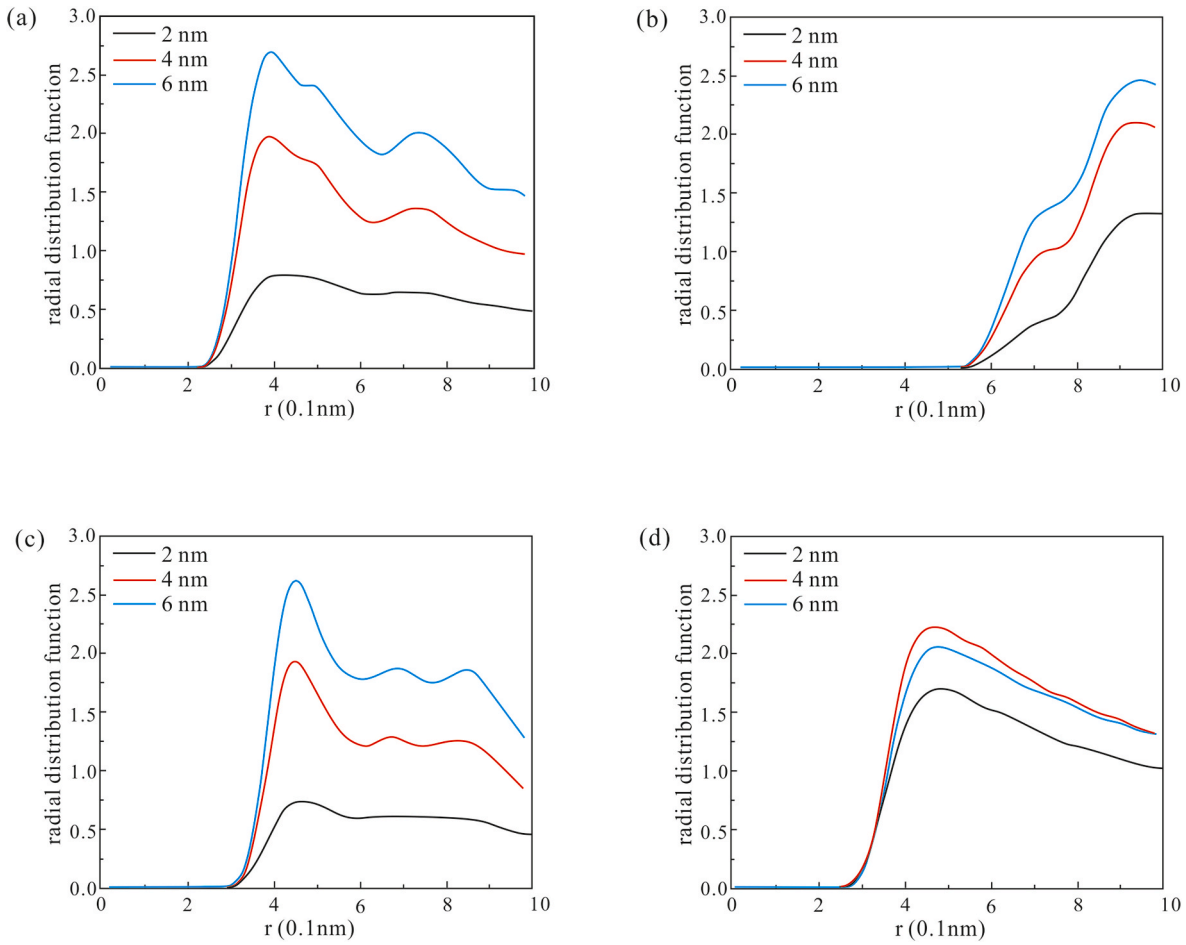

Fig. 12. RDF of methane molecules and each atom at different pore sizes at 298 K and 0.1 MPa. (a) Methane and oxygen; (b) Methane and aluminum; (c) Methane and silicon; (d) Methane and carbon.

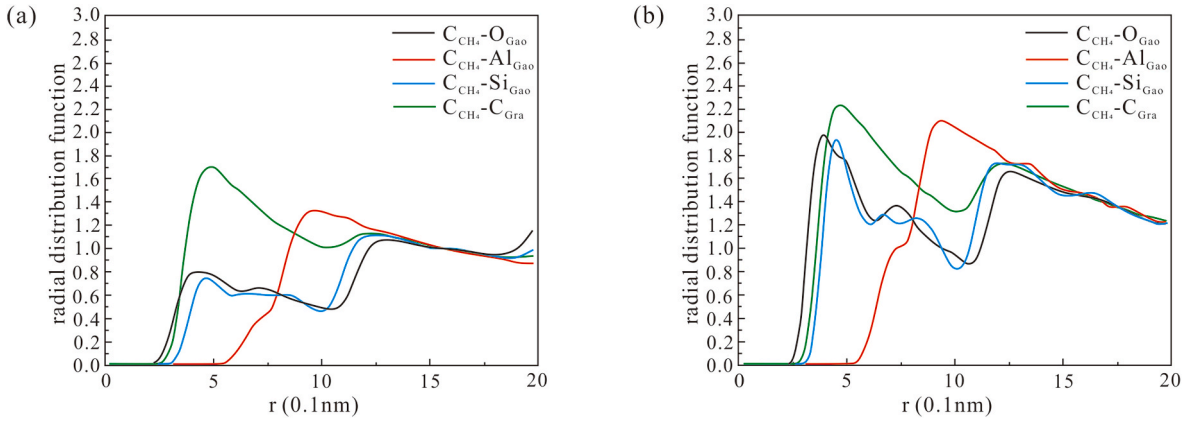

Fig. 13. RDF of methane molecules and each atom at 298 K and 0.1 MPa. (a) The slit aperture is 2 nm; (b) The slit aperture is 4 nm.

the surface of methane molecules and minerals under different pore sizes in this environment. The results are presented in Fig. 12. Methane and kaolinite alumina octahedron surface on the body surface of Al atoms and silicon on the surface of the tetrahedron O, Si, and graphene C atoms between the RDF value increases, its forces increase with the increase in the aperture between. This is because an increase in the aperture increases the adsorption quantity of methane; the increase in the number of methane molecules increases intermolecular van der Waals forces.

Sun H et al. [82] analyzed that different molecules present different interaction intensities in the narrow pores of the same clay mineral. Qwa B et al. [83] believed that there was no obvious peak between methane and each atom in clay minerals, indicating that in the mixture of carbon dioxide and methane, the pore wall of clay minerals had a weak interaction with methane. In our single-component study, the peaks of methane and each atom are very obvious. Under such conditions (Fig. 13), the close contact peak between methane molecules and C atoms of graphene is sharper than that of other atoms on the kaolinite surface, indicating that the substitution sites around C atoms in graphene are high-energy sites of methane molecules in the entire system,

Table 3
Energy changes in the system at different temperatures and pressures when the aperture is 6 nm.

P/MPa	T/K	Van der Waals energy (kcal/mol)			Electrostatic energy (kcal/mol)		
		The aperture is 6 nm					
		Structure optimization	Dynamics	Change	Structure optimization	Dynamics	Change
0.1	298	−22.345	−30.194	−7.849	4.321	−28.628	−32.949
5	323	−154.639	−189.749	−35.11	19.007	−146.836	−165.843
10	348	−359.993	−300.821	59.172	26.938	−246.384	−273.322
15	373	−577.184	−371.051	206.133	40.778	−298.626	−339.404
20	398	−782.954	−430.109	352.845	41.366	−353.296	−394.662

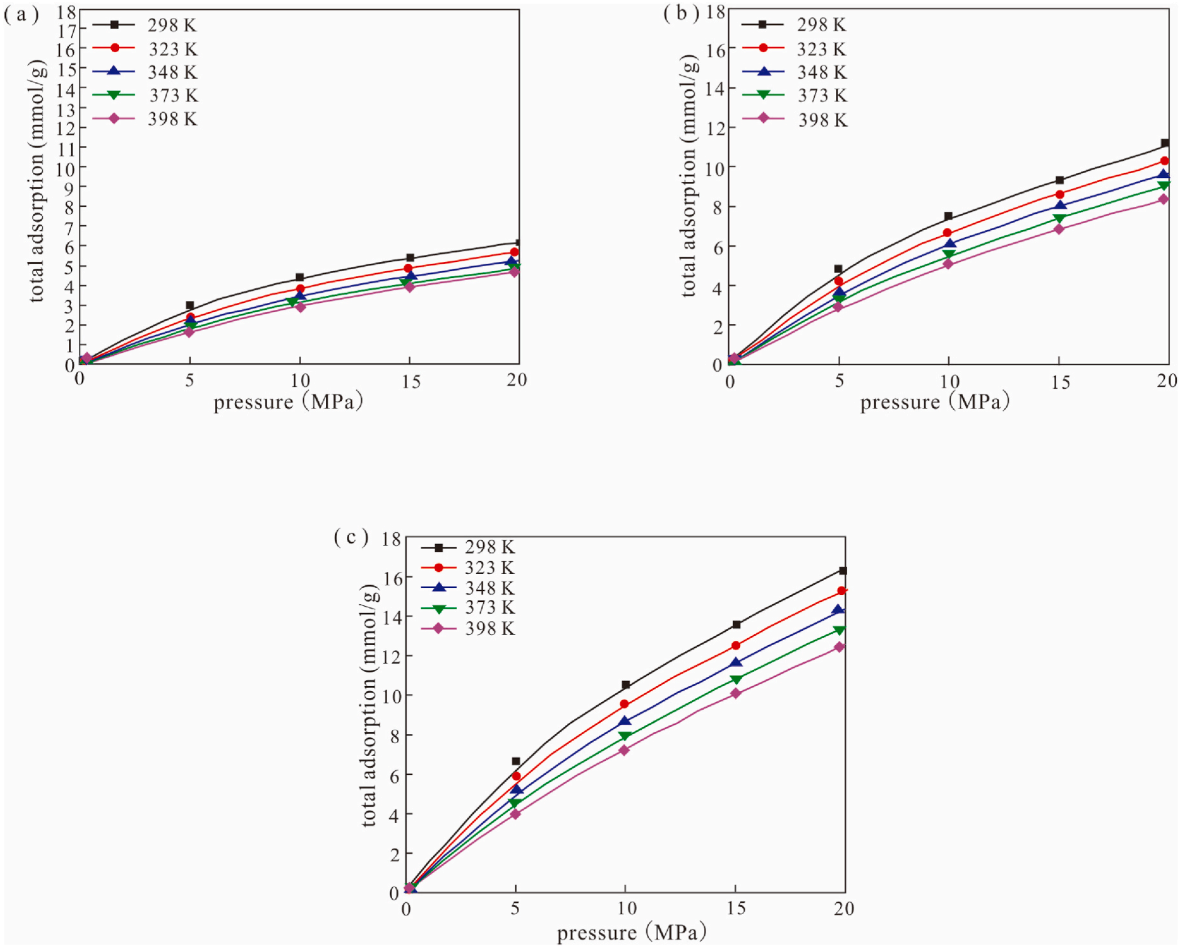

Fig. 14. Absolute isothermal adsorption curves of methane at different pore sizes. (a) The slit aperture is 2 nm; (b) The slit aperture is 4 nm; (c) The slit aperture is 6 nm.

with greater the number of methane molecules surrounding them. On the kaolinite surface, the peaks of O and Si of Al atoms on the octahedral surface of methane and kaolinite alumina are higher than those on the tetrahedral surface of kaolinite silicon, indicating that Al atoms on the octahedral surface of kaolinite alumina are the sub-high-energy sites of methane molecules in the system.

3.4. Energy analysis

Methane molecules can be adsorbed on the pore wall surface because of the joint action of the van der Waals and electrostatic energies [84]. Table 3 lists the changes in the van der Waals and electrostatic energies before and after the molecular dynamics simulation under different temperature and pressure conditions and for a 6-nm pore size. When the temperature and pressure are simultaneously changed, the absolute values of the van der Waals and electrostatic energies are also proportional to these changes. In the temperature and pressure ranges simulated in this work, the van der Waals energy after kinetic simulation first decreased; subsequently, it increased as the system temperature and pressure increased. In other words, the system changes from releasing the van der Waals energy to absorbing it. The amount of van der Waals energy absorbed gradually increases, indicating that the system stability decreases. Compared with the combined influence of temperature and pressure the van der Waals energy, that of only temperature is greater. The system also releases electrostatic energy after methane molecule adsorption. The change in the electrostatic energy is negative, and its absolute value increases, indicating that the energy released by the system also increases, thereby enhancing the structural stability of the system. The influence of pressure on the electrostatic energy is greater than that of temperature control. In general, the relative molecule

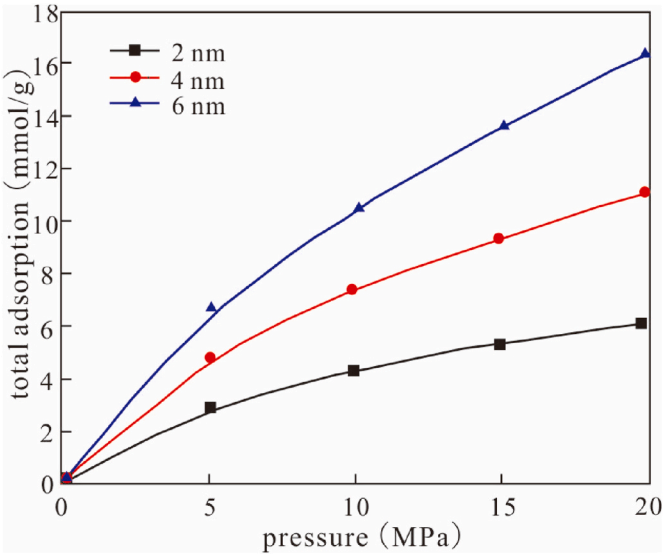

Fig. 15. Total adsorption amount of methane at 298 K and 20 MPa.

concentration shown in Fig. 8 is greatly affected by the temperature. The temperature increase leads to a decrease in the structural stability. The influence of the van der Waals energy on the system is more significant than that of electrostatic energy.

3.5. Changes in adsorption capacity

3.5.1. Total adsorption capacity

In this paper, the total adsorption capacity in the system is obtained via GCMC simulations. The adsorption of methane in slit pores increases first and then becomes stable after reaching the saturation of pore adsorption capacity [85]. The total adsorption isotherms of methane at different pore sizes, a temperature range of 298–398 K, and a pressure range of 0.1–20 MPa were studied (Fig. 14a). The results show that the total adsorption capacity of the system is proportional to the change in pressure; with increasing pressure, the van der Waals force decreases and the effect of electrostatic force increases, thereby increasing the possibility of adsorbate collisions with the shale pore wall, can make the pore wall surface has low adsorption can more molecular adsorption, adsorption sites with an increase to achieve the effect of the adsorption quantity. As shown in Fig. 14b and (c), the total adsorption quantity is inversely proportional to temperature changes because when the temperature is lower, on the surface of the solid adsorption potential energy is larger, the gas molecules will first be attached to the surface, the adsorption gradually occupied, adsorption on the surface of the potential energy is reduced, and with the increase in temperature, increase the adsorption properties of thermal motion and the molecular mean free path between will increase. The limitation effect in the pores is offset, and the adsorption capacity of the solid surface is reduced. More gas molecules will be released on the surface, making adsorption more difficult, thereby reducing the adsorption capacity of the system. Fig. 14 shows that the total adsorption quantity is maximum at 298 K and 20 MPa. Fig. 15 shows the total adsorption isothermal curve of methane with different pore sizes at 298 K. The total methane adsorption quantity

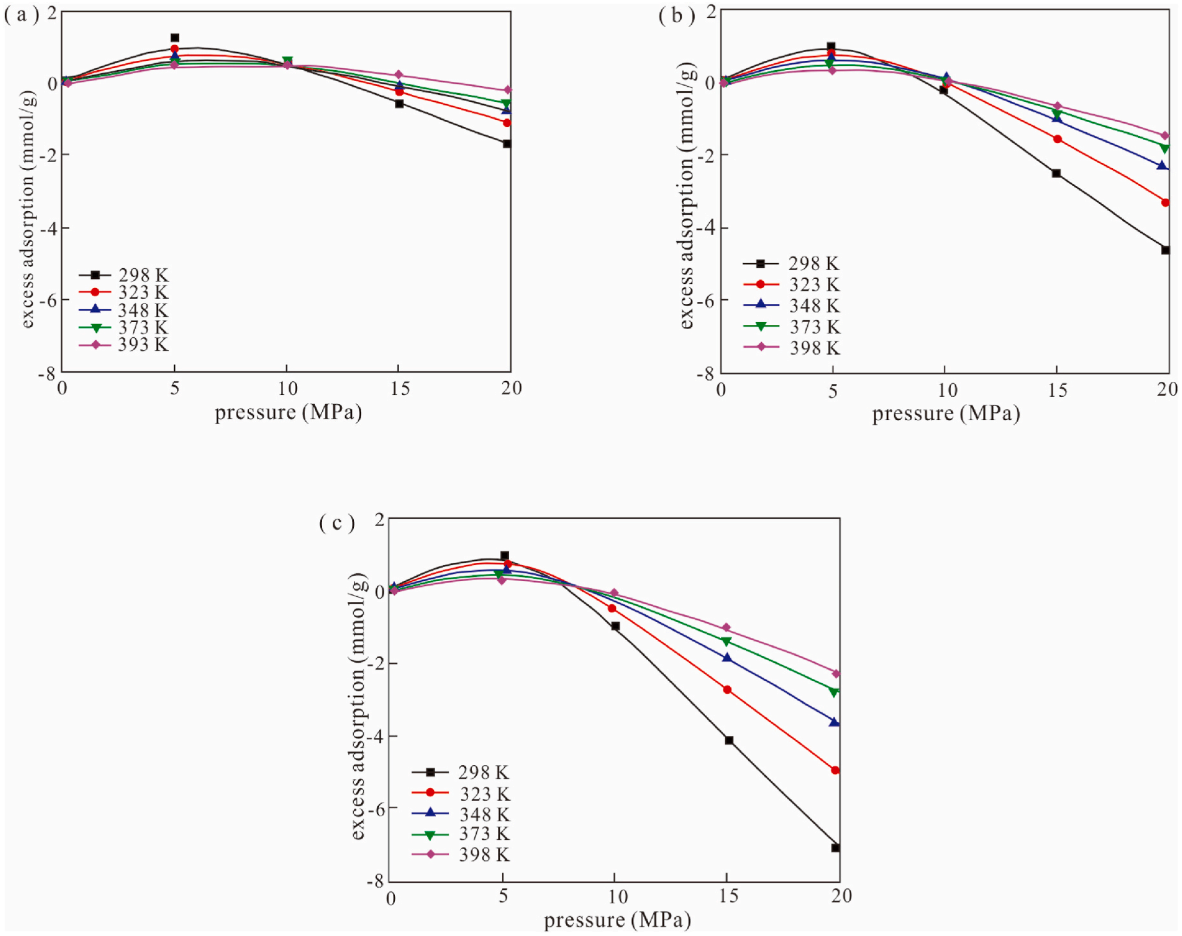

Fig. 16. Variation in excess adsorption capacity of methane at different pore sizes. (a) Slit aperture of 2 nm; (b) Slit aperture of 4 nm; (c) Slit aperture of 6 nm.

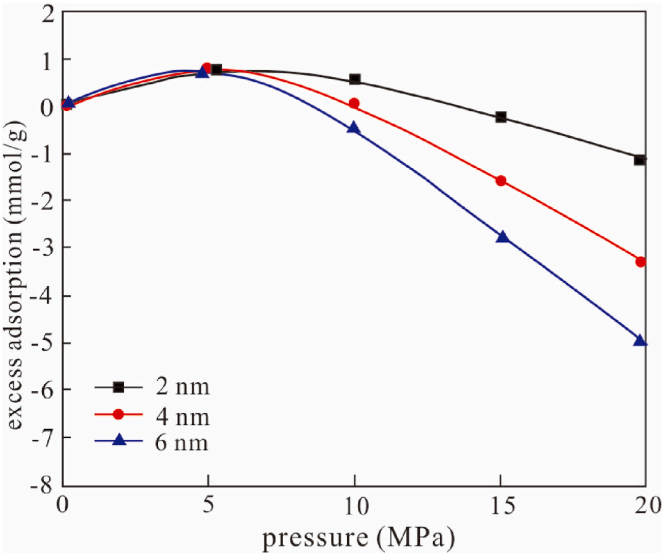

Fig. 17. Variation in excess adsorption capacity of methane at different pore sizes at 323 K.

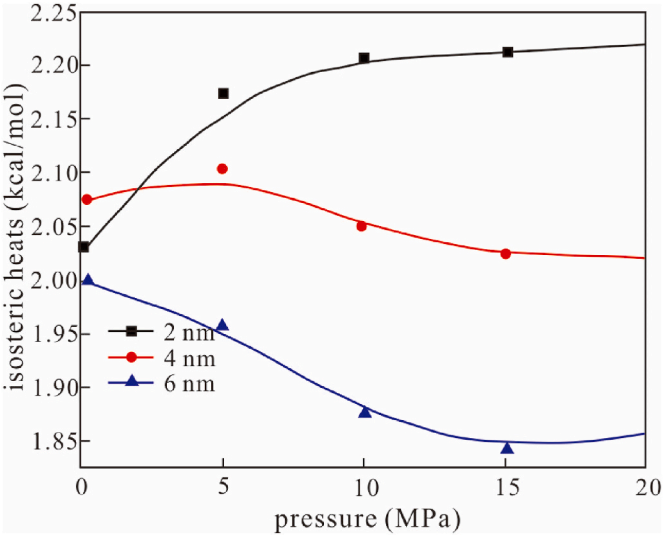

Fig. 18. Variation in adsorption heat with pressure at different pore sizes at 323 K.

increases with increasing aperture. Because an increase in slit aperture to form the adsorption layer has a promoting effect and reduces the interaction force between the adsorbate molecules, molecular interactions produce an exclusion effect, making it more difficult for gas adsorption on both ends of the pore wall, indicating that an increase in the aperture can improve the system's adsorption ability. The results are similar to those of Wang Z H et al. [54,86–88] who studied the adsorption characteristics of methane in slit pores of organic matter.

3.5.2. *Excess adsorption capacity*

Excess adsorption refers to the existence of gas molecules in the pore walls of porous materials during the adsorption phase [89]. Excess adsorption isotherms were calculated from the GCMC simulation results. Under the conditions of different pore sizes and temperatures (as shown in Fig. 16), the isothermal curve of the excess adsorption of methane first increases and then decreases with the change in pressure. The excess adsorption capacity of methane reaches the maximum value at 5 MPa, indicating that 5 MPa is the optimal pressure for methane adsorption and that pressure does not change with the change in pore size and temperature. When the pore diameter is 2 nm, the excess adsorption capacity of methane is inversely proportional to the change in temperature under pressure less than 10 MPa, and when the pressure is greater than 10 MPa, the excess adsorption capacity of methane is directly proportional to the change in temperature, which is called the turning pressure. When the pore diameter is 4 nm, the turning pressure is 9 MPa. When the pore diameter is 6 nm, the turning pressure is 7.5 MPa. Thus, the turning pressure is inversely proportional to the pore diameter. When the temperature is 323 K (Fig. 17), the smaller the pore size, the larger the excess adsorption amount of methane. This is because excess adsorption is closely related to the concentration difference between adsorbed and free methane. The value of excess adsorption is greatest when the concentration difference is greatest. The decrease in excess adsorption is due to the decrease in the concentration difference between adsorbed and free methane with an increase in temperature and pressure. At different pore sizes, the excess adsorption is inversely proportional to the relative concentration of free methane gas. According to the relative concentration distribution diagram, at 323 K, the relative concentration of free methane gas decreases with the increase in pore size, which further increases the excess adsorption capacity. Therefore, the smaller the pore size, the larger the value of the excess adsorption capacity of methane. This is consistent with the conclusion of Xy A et al. [90–92], and the excess adsorption capacity also presents a negative value. However, Wilcox R J et al. [93] argued that the excess adsorption capacity simulated by GCMC at pressures from 2.5 to 20 MPa is a little larger than the actual value. These models have been neglected in molecular simulation studies, but may play an important role in determining the accurate capacity under the nanoscale limitation.

3.6. *Adsorption heat*

The adsorption heat of methane gas reflects the interaction between adsorbent–adsorbate and adsorbant–adsorbate [94–97]. At 323 K, the adsorption heat of the system with an aperture of 2 nm increases with a change in pressure; the adsorption heat of the system with an aperture of 4 nm first increases and then decreases with a change in pressure; the adsorption heat of the system with an aperture of 6 nm decreases first and then increases with increasing pressure (Fig. 18). When the pressure is greater than 2.5 MPa, the change in adsorption heat decreases with increasing pore size. This may be due to the heterogeneity of the pore surface, as methane molecules are more easily adsorbed at high-energy positions. With the increase in the number of methane molecules, the intermolecular van der Waals force becomes stronger and the adsorption heat increases. As presented in Table 4, as temperature and pressure increased, the adsorption heat of the system with a pore diameter of 2 nm increased first, then decreased, and then increased, whereas the adsorption heat of the system with pore diameters of 4 and 6 nm was inversely proportional to the change in temperature and pressure, and both exhibited a slowly decreasing trend. This is because, in mesopores, methane molecules in the system gain more kinetic energy with a gradual increase in temperature, and Brownian motion is intensified, gradually breaking through the adsorption potential barrier on the inner surface of the pore wall. The number of methane molecules entering the free state from the adsorption state increases, decreasing the adsorption heat and gradually approaching the equilibrium state.

4. Conclusions

Based on the actual geological conditions of the Songliao Basin, MD and GCMC simulations were used to analyze the adsorption behavior of methane on the surface of graphene–kaolinite slit pores with pore sizes 2, 4, and 6 nm, at a temperature range of 298–398 K, and a pressure range of 0.1–20 MPa. Through this research, the following conclusions can be drawn:

Table 4
Changes in adsorption heat of methane under different temperatures and pressures.

The aperture width		2 nm			4 nm			6 nm		
P/MPa	T/K	Adsorption heat(kcal/mol)			Adsorption heat(kcal/mol)			Adsorption heat(kcal/mol)		
		Ave	Min	Max	Ave	Min	Max	Ave	Min	Max
0.1	298	2.093	−4.008	3.792	2.179	−1.608	4.192	2.106	2.908	4.292
5	323	2.173	−4.358	5.042	2.103	−5.458	5.242	1.956	4.258	5.442
10	348	2.133	−6.108	4.992	1.978	−5.208	5.492	1.812	5.408	5.492
15	373	2.092	−6.059	5.141	1.912	−6.059	5.541	1.764	5.859	5.841
20	398	2.144	−5.609	5.391	1.875	−5.909	5.591	1.752	7.909	5.791

(1) As temperature and pressure increase, the slope of the root mean square displacement of methane molecules increases gradually, indicating that the kinetic energy of methane in the graphene–kaolinite adsorption system is enhanced, and the molecular thermal motion is intensified. In addition, at constant temperature and pressure, an increase in pore size increases the root mean square displacement of methane molecules.
(2) The relative concentration distribution of methane molecules in graphene–kaolinite slit pores is inversely proportional to the change in temperature and pressure, and the adsorption concentration of methane molecules on the graphene surface is higher than that on the kaolinite surface, indicating that the adsorption capacity of graphene is stronger than that of kaolinite. When the pore size increases gradually to 2, 4, and 6 nm, the peak value of the relative concentration at both ends of the pore wall also increases gradually, but the relative concentration of the first adsorption layer does not increase exponentially with an increase in the pore size.
(3) The close contact peak between methane molecule and C atom in graphene is sharper than other atoms on the surface of kaolinite, indicating that the substituent site around C atom in graphene is the high-energy site of methane molecule in the whole system, and the number of methane molecules around it is more. On the surface of kaolinite, the O and Si peaks of the Al atoms on the surface of methane and kaolinite alumina octahedron are higher than the AI atoms on the surface of kaolinite silicon tetrahedron, indicating that the AI atoms on the surface of kaolinite alumina octahedron are the secondary high-energy sites of methane molecules in the system.
(4) The total adsorption capacity of the adsorption system is proportional to the change of pressure and pore size, and inversely proportional to the change of temperature. In the study of methane excess adsorption, the methane excess adsorption isotherm curve first increases and then decreases, and the methane excess adsorption value increases with the decrease of pore size.

Credit author statement

Junqing Chen, Fujie Jiang: Conceptualization, Methodology, Validation, Writing review & editing. Qi Cong, Xiongqi Pang, Kuiyou Ma, Kanyuan Shi: Investigation, Software, Writing original draft, Data curation, Visualization. Bo Pang, Dongxia Chen, Hong Pang: Supervision, Conceptualization. Xiaobin Yang, Yuying Wang, Bingyao Li: Software.

Declaration of competing interest

The authors declare that they have no known competing financial interests or personal relationships that could have appeared to influence the work reported in this paper.

Data availability

No data was used for the research described in the article.

Acknowledgments

This work was supported by the National Natural Science Foundation of China (Grant number 42102145); the Science Foundations of China University of Petroleum, Beijing (Grant number 2462022YXZZ007); and the Joint Fund of the National Natural Science Foundation of China (Grant Number U19B6003-02-04).

References

[1] Fan CJ, Elsworth D, Li S. Zhou L.J., Yang Z.H., Song Y. Thermo-hydro-mechanical-chemical couplings controlling CH4 production and CO2 sequestration in enhanced coalbed methane recovery. Energy 2019;173:1054–77. https://doi.org/10.1016/j.energy.2019.02.126.
[2] Sharma A, Namsani S, Singh JK. Molecular simulation of shale gas adsorption and diffusion in inorganic nanopores. Mol Simulat 2015;41(5–6):414–22. https://doi.org/10.1080/08927022.2014.968850.
[3] Zhai ZQ, Wang XQ, Jin X, Sun L, Li JM, Cao DP. Adsorption and diffusion of shale gas reservoirs in modeled clay minerals at different geological depths. Energy Fuel 2014;28(12):7467–73. https://doi.org/10.1021/ef 5023434.
[4] Kadoura A, Nair AKN, Sun SY. Molecular dynamics simulations of carbon dioxide, methane, and their mixture in montmorillonite clay hydrates. J Phys Chem C 2016;120(23):12517–29. https://doi.org/10.1021/acs.jpcc.6b02748.
[5] Pan Z, Connell LD. Reservoir simulation of free and adsorbed gas production from shale. J Nat Gas Sci Eng 2015;22:359–70. https://doi.org/10.1016/j.jngse.2014.12.013.
[6] Curtis JB. Fractured shale-gas systems. AAPG Bull 2002;86(11):1921–38. https://doi.org/10.1306/61EEDDBE-173E-11D7-8645000102C1865D.
[7] Degance AE, Morgan WD, Yee D. Fluid Phase Equil 1993;82:215–24.
[8] McGlade C, Speirs J, Sorrell S. Methods of estimating shale gas resources - comparison, evaluation and implications. Energy 2013;59:116–25. https://doi.org/10.1016/j.energy.2013.05.031.
[9] Xiong J, Liu X, Liang L. Experimental study on the pore structure characteristics of the Upper Ordovician Wufeng Formation shale in the southwest portion of the Sichuan Basin, China. J Nat Gas Sci Eng 2015;22:530–9. https://doi.org/10.1016/j.jngse.2015.01.004.
[10] Zhang S, Liu Q, Cheng H, Li X, Zeng F, Frost RL. Intercalation of dodecylamine into kaolinite and its layering structure investigated by molecular dynamics simulation. J Colloid Interface Sci 2014;430:345–50. https://doi.org/10.1016/j.jcis.2014.05.059.
[11] Joffe J. Fugacities in gas mixtures. Energy Pol 1948;34:2848–57. https://doi.org/10.1021/ie50465a029.
[12] Leach AR. Molecular modeling : principle and application. London: Addison Wesley Longman Limited; 1996. p. 12–20.
[13] Yu QS, Zhu LG. An introduction to molecular design. Beijing: China Higher Education Press; 2000. p. 24–35.
[14] Deng Z, Yi W, Li GZ, Li AQ, Wang B, Geng D. Research on prediction method of residual gas content in coal. Theory and Technology of Coalbed methane exploration and Development-Proceedings of 2010 National Coalbed Methane. Academic Conference; 2010.
[15] Dong Q, Liu XP, Li WG. Discussion on determination method of shale gas content. Natural gas & oil 2012;30(5):34–7.
[16] Zhao YJ, Guo W, Xiong W. Nat Gas Geosci 2014;25(6):940–6.
[17] Yu J, Xie LH, Li JR. CO2 capture and separations using MOFs: computational and experimental studies. Chem Rev 2017;117:9674–754. https://doi.org/10.1021/acs.chemrev.6b00626.
[18] Chen JY. Application of low-field NUCLEAR magnetic resonance technology in shale adsorption. Beijing: China University of Geosciences; 2016. p. 10–26. https://doi.org/10.27493/d.cnki.gzdzy.2016.000105.
[19] Gong HJ, Jin L, Zhu CF, Qian S, Li YJ, Dong MZ. Laboratory research and exploration 2020;39(2):12–15+33.

[20] Metropolis N, Rosenbluth AW, Rosenbluth MN. Equation of state calculations by fast computing machines. J Chem Phys 2004;21(6):1087–92. https://doi.org/10.1063/1.1699114.

[21] Zhou SW, Wang HY, Xue HQ. Comparative analysis of calculation methods of gas loss in shale gas content field Test13. China Science and Technology Paper; 2018. p. 2453–60.

[22] Liu N, Ma J. Zan C.L. Measurement and Method Discussion of Shale Gas Content in the Ordos Basin.Complex Oil and Gas. Reservoirs 2014;7(03):5–10.

[23] Wang ZY, Peng WQ, Song ZR. Influence factors of field analytical volume of shale gas: a case study of Well Changyecan 1, Weibei Sag. Shandong Land and Resources 2015;31(9):22–5.

[24] Feng QQ, Qiu NS, Borjigin Wu H, Zhang JT, Shen BJ, Wang JS T. Tectonic evolution revealed by thermo-kinematic and its effect on shale gas preservation. Energy 2022;240:122781. https://doi.org/10.1016/j.energy.2021.122781.

[25] Yang F, Ning ZF, Liu HQ. Research on isothermal adsorption characteristics of shale to shale gas. Special Oil Gas Reservoirs 2013;20(5):133–6.

[26] Duan XG, Hu ZM, Nan S. Establishment of a new slip permeability model of gas flow in shale nanopores based on experimental and molecular dynamics simulations studies. J Petrol Sci Eng 2020;193:107365. https://doi.org/10.1016/j.petrol.2020.107365.

[27] Ji L, Zhang T, Milliken KL, Qu J, Zhang X. Experimental investigation of main controls to methane adsorption in clay-rich rocks. Appl Geochem 2012;27:2533–45. https://doi.org/10.1016/j.apgeochem.2012.08.027.

[28] Sharma A, Namsani S, Singh JK. Molecular simulation of shale gas adsorption and diffusion in inorganic nanopores. Mol Simulat 2015;41:414–22. https://doi.org/10.1080/08927022.2014.968850.

[29] Huang L. Molecular simulation of adsorption behaviors of methane, carbon dioxide and their mixtures on kerogen: effect of kerogen maturity and moisture content. Fuel 2018;211:159–72. https://doi.org/10.1016/j.fuel.2017.09.060.

[30] Li Y. Alkanes adsorption and flow molecular simulation in tight carbonate reservoirs. Southwest Petroleum University 2016:11–9.

[31] Song W, Yao J, Ma J. Grand canonical Monte Carlo simulations of pore structure influence on methane adsorption in micro-porous carbons with applications to coal and shale systems. Fuel 2018;215:196–203.

[32] Wang S, Javadpour F, Feng Q. Fast mass transport of oil and supercritical carbon dioxide through organic nanopores in shale. Fuel 2016;181:741–58. https://doi.org/10.1016/j.fuel.2016.05.057.

[33] Mosher K, He J, Liu Y, Rupp E, Wilcox J. Molecular simulation of methane adsorption in micro- and mesoporous carbons with applications to coal and gas shale systems. Int J Coal Geol 2013;109(3):6–44. https://doi.org/10.1016/j.coal.2013.01.001.

[34] Cao XM. Pore characteristics and evolution of late cretaceous Qingshankou Formation shale in Songliao Basin. Beijing: China University of Geosciences; 2020;12-21. https://doi.org/10.27493/d.cnki.gzdzy.2020.001451.

[35] Riewchotisakul S, Akkutlu IY. Adsorption-enhanced transport of hydrocarbons in organic nanopores. SPE J 2016;21:1960–9. https://doi.org/10.2118/175107-PA.

[36] Lin K, Yuan Q, Zhao YP. Using graphene to simplify the adsorption of methane on shale in MD simulations. Comput Mater Sci 2017;133:99–107. https://doi.org/10.1016/j.commatsci.2017.03.010.

[37] Zhang L, Wang CJ, Yan ZF, Wu XL, Wang YQ, Meng DW, Xie HX. Kaolinite nanomaterial: intercalation of 1-butyl-3-methylimidazolium bromine in a methanol–kaolinite pre-intercalate. Appl Clay Sci 2013;86:106–10. https://doi.org/10.1016/j.clay.2013.07.003.

[38] Zhang S, Liu Q, Cheng H. Intercalation of dodecylamine into kaolinite and its layering structure investigated by molecular dynamics simulation. J Colloid Interface Sci 2014;430(5):345–50. https://doi.org/10.1016/j.jcis.2014.05.059.

[39] Chen SB, Zhu YM, Wang HY, Liu HL, Wei W, Fang JH. Mineral composition characteristics and significance of shale gas reservoirs in lower silurian longmaxi formation, southern margin of sichuan basin. Acta Pet Sin 2011;32(5):775–82.

[40] Chen S, Zhu Y, Wang H. Shale gas reservoir characterisation: a typical case in the southern Sichuan Basin of China. Energy 2011;36(11):6609–16. https://doi.org/10.1016/j.energy.2011.09.001.

[41] Cao DP, Zhang XR, Chen JF, Wang WC, Yun J. Optimization of single-walled carbon nanotube arrays for methane storage at room temperature. J Phys Chem B 2003;107:13286–92. https://doi.org/10.1021/jp036094r.

[42] Foerster J, Lansford J, Laskar J, Rappaport T, Kato S. High uptakes of methane in Li-doped 3D covalent organic frameworks. Langmuir Acs J. Surf. Colloids 2010;26:220–6. https://doi.org/10.1021/la9020383.

[43] Xia H, Wang FZ, Xue-Qiang LI. Preparation and characterization of kaolinite potassium acetate intercalation comple. J Harbin Inst Technol 2006;38(1):126–9.

[44] Zhang L, Wang CJ, Yan ZF. Kaolinite nanomaterial: intercalation of 1butyl-3-methylimidazolium bromine in a methanol–kaolinite pre-intercalate. Appl Clay Sci 2013;86(8):106–10.

[45] Zhang S, Tang S, Zheng Q. Evaluation of geological features for deep coalbed methane reservoirs in the Dacheng Salient, Jizhong Depression, China. Int J Coal Geol 2014;133:60–71. https://doi.org/10.1016/j.coal.2014.09.002.

[46] Zhang J, Clennell MB, Dewhurst DN. Combined Monte Carlo and molecular dynamics simulation of methane adsorption on dry and moist coal. Fuel 2014;122(15):186–97. https://doi.org/10.1016/j.fuel.2014.01.006.

[47] Sun RY, Zhang YF, Fan KK. Molecular simulation of adsorption characteristics of clay minerals in shale. Journal of chemical industry 2015;66(06):2118–22.

[48] Hu H, Li X, Fang Z, Wei N, Li Q. Small-molecule gas sorption and diffusion in coal: molecular simulation. Energy 2010;35:2939–44. https://doi.org/10.1016/j.energy.2010.03.028.

[49] Xiang J, Zeng F, Liang H, Li B, Song X. Molecular simulation of the CH4/CO2/H2O adsorption onto the molecular structure of coal. Science China. Earth Sci 2014;44(07):1418–28.

[50] Zhang J, Clennell M, Dewhurst D, Liu K. Combined Monte Carlo and molecular dynamics simulation of methane adsorption on dry and moist coal. Fuel 2014;122:186–97. https://doi.org/10.1016/j.fuel.2014.01.006.

[51] Mosher K, He J, Liu Y, Rupp E, Wilcox J. Molecular simulation of methane adsorption in micro-and mesoporous carbons with applications to coal and gas shale systems. Int J Coal Geol 2013;109:36–44.

[52] Peng DY, Robinson DB. A new two-constant equation of state. Ind Eng Chem Fundam 1976;15:92–4.

[53] Zhang J, Liu K, Clennell MB, Dewhurst DN, Pervukhina M. Molecular simulation of CO2–CH4 competitive adsorption and induced coal swelling. Fuel 2015;160:309–17.

[54] Sui H, Yao J, Zhang L. Molecular simulation of shale gas adsorption and diffusion in clay nanopores. Computation 2015;3:687–700. https://doi.org/10.3390/computation3040687.

[55] Mosher K, He J, Liu Y, Rupp E, Wilcox J. Molecular simulation of methane adsorption in micro- and mesoporous carbons with applications to coal and gas shale systems. Int. J. Coal Geol. 2013;109-110:36–44. https://doi.org/10.1016/j.coal.2013.01.001.

[56] Krishna R, Baten JMV. Investigating the potential of MgMOF-74 membranes for CO2 capture. J Membr Sci 2011;377:249–60.

[57] Zou CN, Dong DZ, Wang SJ. Geological characteristics and resource potential of shale gas in China. Petrol Explor Dev 2010;37(6):641–53. https://doi.org/10.1016/S1876-3804(11)60001-3.

[58] Lu SF, Huang WB, Chen FW. Classification and evaluation criteria of shale oil and gas resources : discussion and application. Petrol Explor Dev 2012;39(2):268–76. https://doi.org/10.1016/S1876-3804(12)60042-1.

[59] Li XJ, Xu H. Feasibility analysis on MC simulation in coalbed methane adsorption and desorption. Coal Technol 2010;29(9):84–6.

[60] Cao D, Wu J. Self-diffusion of methane in single-walled carbon nanotubes at sub- and supercritical conditions. Langmuir 2004;20(9):3759–65.

[61] Yang X, Zhang C. Structure and diffusion behavior of dense carbon dioxide fluid in clay-like slit pores by molecular dynamics simulation. Chem Phys Lett 2005;407(4–6):427–32. https://doi.org/10.1016/j.cplett.2005.03.118.

[62] Sun H. COMPASS:An ab initio force-field optimized for condensed-phase applications overview with details on alkane and benzene compounds. J Phys Chem B 1998;5647(98):7338–7364..

[63] Sun H, Ren P, Fried JR. The COMPASS Force-Field: parameterization and validation for phosphazenes. Comput Theor Polym Sci 1998;8(1–2):229–46.

[64] Andersen HC. Molecular dynamics simulations at constant pressure and/or temperature. J Phys Chem 1980;72(4):2384–93. https://doi.org/10.1063/1.439486.

[65] Jiao H, Dong M, Liu Z. Molecular dynamics simulation of methane adsorption with presence of water on different wettability quartz surface. Journal of China University of Petroleum(Natural science edition 2014;38(5):178–83. https://doi.org/10.1016/j.micromeso.2016.01.010.

[66] Kadoura A, Nair AKN, Sun S. Adsorption of carbon dioxide, methane, and their mixture by montmorillonite in the presence of water. Microporous Mesoporous Mater 2016;225:331–41.

[67] Lu YG, Peng JX. Study of acoustical properties of supercritical carbon dioxide using liquid acoustical theory. Acta Phys Sin 2008;57(2):1030–6.

[68] Li HY, Fu G, Peng SM. Experimental study on the diffusion coefficients of natural gas. Petroleum Geology & Experiment 2001;23(1):108–12.

[69] CAO W, LÜ LH, HUANG LL, WANG SS. ZHU Y.D.Molecular simulations on diameter effect of carbon nanotube for separation of CO2/CH4. CIE J 2014;65(5):1736–42.

[70] Zhang XL, Kang YL. Influence factors analysis of shale methane diffusion coefficient//The Chinese mechanical assembly 2013. Xi'an: Abstract Set; 2013. p. 154–5.

[71] Liu GD, Zhao ZY, Sun ML. New insights into natural gas diffusion coefficient in rocks. Petrol Explor Dev 2012;39(5):559–65.

[72] Skoulidas AI, Ackerman DM, Johnson JK, Sholl DS. Rapid transport of gases in carbon nanotubes. Phys Rev Lett 2002;89(18):185901.

[73] Kim C, Jang H, Lee J. Experimental investigation on the characteristics of gas diffusion in shale gas reservoir using porosity and permeability of nanopore scale. J Pet Sci Eng 2015;133:226–37. https://doi.org/10.1016/j.petrol.2015.06.008.

[74] Bhatia SK, Nicholson D. Adsorption and diffusion of methane in silica nanopores: a comparison of single-site and five-site models. J Phys Chem C 2012;116:2344–55. https://doi.org/10.1021/jp210593d.

[75] Kazemi M, Takbiri-Borujeni A. Modeling and simulation of gas transport in carbon-based organic nano-capillaries. Fuel 2017;206(oct.15):724–37. https://doi.org/10.1016/j.fuel.2017.04.033.

[76] Zhang T, He Y, Yang Wu K Y. Molecular simulation of shale gas adsorption in organic-matter nanopore. Journal of Natural Gas Geoscience 2018;2(5). https://doi.org/10.1016/j.jnggs.2018.01.001.

[77] Chen C, Hu W, Sun Li W, Song Y J. CH4 adsorption and diffusion in shale pores from molecular simulation and a model for CH4 adsorption in shale matrix. Int J Heat Mass Tran 2019;141(OCT):367. https://doi.org/10.1016/j.ijheatmasstransfer.2019.06.087.

[78] Sharma A, Namsani S, Singh JK. Molecular simulation of shale gas adsorption and diffusion in inorganic nanopores. Mol Simulat 2015;41(5–6):414–22. https://doi.org/10.1080/08927022.2014.968850.

[79] Zhang B, Kang J, Kang T. Monte Carlo simulations of methane adsorption on kaolinite as a function of pore size. J Nat Gas Sci Eng 2018;49:410–6.

[80] Wu HA, Chen J, Liu H. Molecular dynamics simulations about adsorption and displacement of methane in carbon nanochannels. J Phys Chem C 2015;119(24): 150527003615009. https://doi.org/10.1021/acs.jpcc.5b02436.
[81] Jin Z, Firoozabadi A. Effect of water on methane and carbon dioxide sorption in clay minerals by Monte Carlo simulations. Fluid Phase Equil 2014;382:10–20. https://doi.org/10.1016/j.fluid.2014.07.035.
[82] Sun H, Zhao H, Qi Li Y N Qi XQ. Molecular insight into the micro-behaviors of CH 4 and CO 2 in montmorillonite slit-nanopores. Mol Simulat 2017;43(13–16):1–8. https://doi.org/10.1080/08927022.2017.1328553.
[83] Qwa B, Liang H. Molecular insight into competitive adsorption of methane and carbon dioxide in montmorillonite: effect of clay structure and water content - ScienceDirect. Fuel 2019;239:32–43. https://doi.org/10.1016/j.fuel.2018.10.149.
[84] Bhatia SK, Nicholson D. Adsorption and diffusion of methane in silica nanopores: a comparison of single-site and five-site models. J Phys Chem C 2012;116(3): 2344–55. https://doi.org/10.1021/jp210593d.
[85] Xiong J, Liu X, Liang L, Zeng Q. Adsorption of methane in organic-rich shale nanopores: an experimental and molecular simulation study. Fuel 2017;200: 299–315. https://doi.org/10.1016/j.fuel.2017.03.083.
[86] Wang ZH, Hu SD, Guo P, et al. Molecular simulations of the adsorption of shale gas in organic pores. Mater Res Innovat 2015;19(suppl.5):S5.106–11.
[87] Yuan WN, Pan ZJ, Xiao L, Yang YX, Zhao CX, Connell LD, et al. Experimental study and modelling of methane adsorption and diffusion in shale. Fuel 2014;117: 509–19.
[88] Wang S, Feng Q, Zha M, et al. Supercritical methane diffusion in shale nanopores: effects of pressure, mineral types, and moisture content. Energy & Fuels; 2018; 32 (1):169–180. https://doi.org/10.1021/acs.energyfuels.7b02892.
[89] He S, Palmer JC, Qin G. A non−equilibrium molecular dynamics study of methane transport in clay nano−pores. Microporous Mesoporous Mater 2017;249:88–96.
[90] Yu YR, Li J, Chen ZX, Wu KL. Zhang L.Y.Effects of an adsorbent accessible volume on methane adsorption on shale -. ScienceDirect. Comput Methods Appl Mech Eng 2020;370:113222. https://doi.org/10.1016/j.cma.2020.113222.
[91] Chen GH, Lu SF, Zhang JF, Xue QZ, Han TC, Xu HT, et al. Xu C.X.,Pervukhina M. Keys to linking GCMC simulations and shale gas adsorption experiments[J]. Fuel 2017;199:14–21. https://doi.org/10.1016/j.fuel.2017.02.063.
[92] Wang S, Feng Q, Javadpour F, Hu Q. Wu K.L. Competitive adsorption of methane and ethane in montmorillonite nanopores of shale at supercritical conditions: a grand canonical Monte Carlo simulation study. Chem Eng J 2019;355:76–90. https://doi.org/10.1016/j.cej.2018.08.067.
[93] Wilcox RJ. Molecular simulation of methane adsorption in micro- and mesoporous carbons with applications to coal and gas shale systems. Int J Coal Geol 2013; 109-110: 36-44. https://doi.org/10.1016/j.coal.2013.01.001.
[94] Huang L, Ning Z, Wang Q, Qi R, Li J, Zeng Y. Thermodynamic and structural characterization of bulk organic matter in Chinese Silurian shale: experimental and molecular modeling studies. Energy & Fuels 2017;31(5):4851–65. https://doi.org/10.1021/acs.energyfuels.7b00132.
[95] Shi KY, Chen JQ, Pang Jiang FJ, Hui SS, Pang H, Ma KY, Cong Q XQ. Effect of wettability of shale on CO2 sequestration with enhanced gas recovery in shale reservoir: implications from molecular dynamics simulation. J Nat Gas Sci Eng 2022;107:104798. https://doi.org/10.1016/j.jngse.2022.104798.
[96] Shi KY, Chen JQ, Pang Jiang FJ, Hui SS, Zhao ZC, Chen D, Cong Q, Wang T, Xiao HY, Yang XB, Wang YY XQ. Molecular dynamics simulation of surface wettability of different clay minerals in shale. Petroleum Science; 2023;20(2):689-704. https://doi.org/10.1016/j.petsci.2023.02.001.
[97] Cong Q, Chen JQ, Lu GW, Jiang FJ, Pang B, Shi KY, et al. A review on the influence factors and microscopic mechanism of adsorption capacity of shale by molecular dynamics simulation. J Cent S Univ 2022;53(9):3474–89.